On the space-time difference of proton and composite particle emission in central heavy-ion reactions at 400 $A \cdot$ MeV

The FOPI Collaboration

R. Kotte[5], H. W. Barz[5], W. Neubert[5], C. Plettner[5], D. Wohlfarth[5], J. P. Alard[3], A. Andronic[1], R. Averbeck[4], Z. Basrak[12], N. Bastid[3], N. Bendarag[3], G. Berek[2], R. Čaplar[12], N. Cindro[12], P. Crochet[3], A. Devismes[4], P. Dupieux[3], M. Dželalija[12], M. Eskef[6], Z. Fodor[2], A. Gobbi[4], Y. Grishkin[7], N. Herrmann[6], K. D. Hildenbrand[4], B. Hong[9], J. Kecskemeti[2], Y.J. Kim[9], M. Kirejczyk[11], M. Korolija[12], M. Kowalczyk[11], T. Kress[4], R. Kutsche[4], A. Lebedev[7], K.S. Lee[9], Y. Leifels[6], V. Manko[8], H. Merlitz[6], D. Moisa[1] A. Nianine[8], D. Pelte[6], M. Petrovici[1], F. Rami[10], W. Reisdorf[4], B. de Schauenburg[10], D. Schüll[4], Z. Seres[2], B. Sikora[11], K.S. Sim[9], V. Simion[1], K. Siwek-Wilczyńska[11], A. Somov[7], G. Stoicea[1], M. A. Vasiliev[8], P. Wagner[10], K. Wiśniewski[11], J.T. Yang[9], Y. Yushmanov[8], A. Zhilin[7]

[1] Institute for Nuclear Physics and Engineering, Bucharest, Romania
[2] Central Research Institute for Physics, Budapest, Hungary
[3] Laboratoire de Physique Corpusculaire, Université Blaise Pascal, Clermont-Ferrand, France
[4] Gesellschaft für Schwerionenforschung, Darmstadt, Germany
[5] Forschungszentrum Rossendorf, PF 510119, 01314 Dresden, Germany, (e-mail: `kotte@fz-rossendorf.de`)
[6] Physikalisches Institut der Universität Heidelberg, Heidelberg, Germany
[7] Institute for Experimental and Theoretical Physics, Moscow, Russia
[8] Kurchatov Institute for Atomic Energy, Moscow, Russia
[9] Korea University, Seoul, Korea
[10] Institut de Recherches Subatomiques, IN2P3-CNRS/ULP, Strasbourg, France
[11] Institute of Experimental Physics, Warsaw University, Warsaw, Poland
[12] Rudjer Bošković Institute Zagreb, Zagreb, Croatia

Abstract. Small-angle correlations of pairs of nonidentical light charged particles produced in central collisions of heavy ions in the $A = 100$ mass region at a beam energy of 400 A·MeV are investigated with the FOPI detector system at GSI Darmstadt. The difference of longitudinal correlation functions with the relative velocity parallel and anti-parallel to the center-of-mass velocity of the pair in the central source frame is studied. This method allows extracting the apparent space-time differences of the emission of the charged particles. Comparing the correlations with results of a final-state interaction model delivers quantitative estimates of these asymmetries. Time delays as short as 1 fm/c or – alternatively – source radius differences of a few tenth fm are resolved. The strong collective expansion of the participant zone introduces not only an apparent reduction of the source radius but also a modification of the emission times. After correcting for both effects a complete sequence of the space-time emission of p, d, t, ^{3}He, α particles is presented for the first time.

PACS. 25.70.Pq Multifragment emission and correlations

1 Introduction

Correlations of two nonidentical particles at small relative velocities are – due to final state interactions – sensitive to the space-time structure at freeze-out. Usually, the correlation is used to extract the size of the source and the time duration of the emission [1–7]. However, it contains also information on the emission time differences of the two particles. Gelderloos and Alexander proposed to construct velocity difference spectra at small relative

angles [8]. Comparing these spectra with results of trajectory model calculations they were able to infer the emission order and the time intervals between the emission of the two particles [9]. If the faster particle of a pair approaches and passes the other one from behind the pair experiences a stronger final-state interaction than in the case that the faster particle has started in front of the slower one. Thus, the ratio of the correlation functions with the relative velocity parallel and anti-parallel to the pair velocity is related to the formation sequence.

For heavy-ion collisions of a few hundred MeV per nucleon mainly nucleons and light composite particles with charge number $Z \leq 2$ are emitted, and one expects relative short time differences. For these light ejectiles classical trajectory calculations are not accurate as quantum effects dominate at momenta larger than $\hbar/a_0$ where a_0 is the Bohr radius. Very recently, Lednický et al. [10] have proposed to use the above sensitivity of the correlation function to directly measure the space-time differences in the emission of particles of different types. This is possible since the wave functions for nonidentical particles are asymmetric with respect to the forward and backward direction of the relative momentum. First theoretical [11] and experimental work [12] concentrated on the determination of the asymmetry of particle production of proton-pion pairs. In the present work the proposed method is applied to measure the pair-wise space-time differences of different light charged particles. Applying directional cuts on all relative-velocity correlation functions of nonidentical particles allows one to determine – even with a certain redundancy – the whole sequence of space-time emission points of p, d, t, ^{3}He, and α particles.

The two-particle correlations are sensitive to the spatial separation of the two particles at the time when the second of them freezes out. This separation is the sum of the spatial separation between the two freeze-out points, and the time separation, multiplied by the velocity of the first particle. A correlation measurement does not allow to disentangle these two components. Therefore, in the following investigation we will discuss two cases, first that all particles are emitted from the same region and second that they emerge at the same time instant.

2 The experiment

2.1 Detector setup

The experiment has been performed at the heavy-ion synchrotron SIS at GSI Darmstadt. Targets of 1 % interaction thickness of ^{96}Ru and ^{96}Zr have been irradiated by ^{96}Ru and ^{96}Zr ions of $400A$·MeV beam energy. In order to get sufficient statistics, the data of all target-projectile combinations have been used. The original aim of the utilization of target and projectile nuclei with equal mass but different isospin content was to answer the question whether the colliding nuclear system attains a full thermo-chemical equilibrium during the collision process. The first experimental results reveal substantial transparency effects in phase space regions already slightly apart of midrapidity [13].

The present analysis uses a subsample of the data, taken with the outer Plastic Wall/Helitron combination of the FOPI detector system [14]. The Plastic Wall delivers – via energy loss vs. time-of-flight (TOF) measurement – the nuclear charge Z and the velocity β of the particles. The Helitron gives the curvature (which is a measure of the momentum over charge (p/Z)) of the particle track in the field of a large superconducting solenoid. Since the momentum resolution of the Helitron is
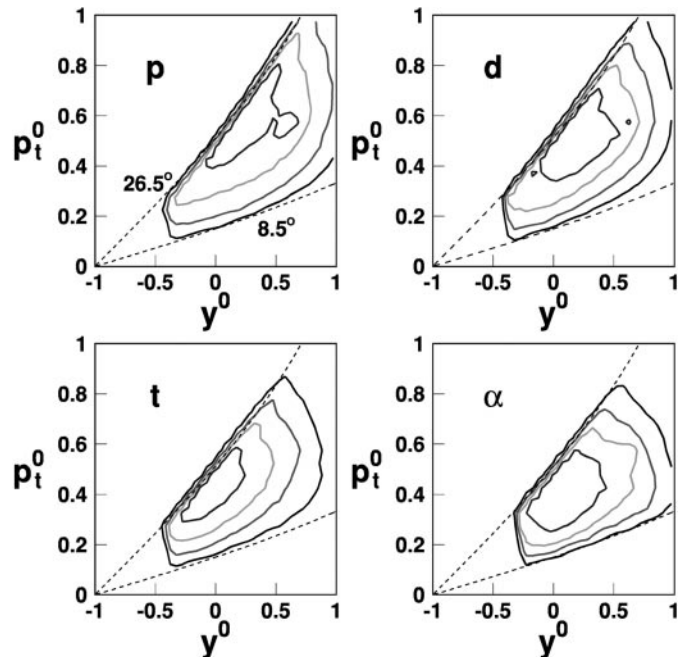

Fig. 1. Two-dimensional distribution of yields $d^2\sigma/dp_t dy$ of p, d, t, α particles in the $p_t^0 - y^0$ plane for central reactions selected by a 8 % cut on large charged particle multiplicities. Target and projectile rapidities are given by $y^0 = -1$ and $+1$, respectively. The full lines are levels of constant yield of 20, 40, 60, and 80 % of the maximum value. Dashed lines represent the polar angle limits at 8.5 and 26.5 degrees

rather moderate, this detector component serves for particle identification only. The mass m is determined via $mc = (p/Z)_{Hel}/(\beta\gamma/Z)_{PlaWa}$, where $\gamma = (1 - \beta^2)^{-1/2}$. The Plastic Wall and the Helitron have full overlap only for polar angles between 8.5 degrees and 26.5 degrees. The corresponding flight paths amount to 450 cm and 380 cm, respectively. Monte-Carlo simulations have been performed in order to study the influence of the finite detector granularity and of the TOF and position resolutions on the velocity and finally on the proton momentum. The resolution of both quantities is governed by the TOF resolution, which is $\sigma_{TOF} = 80$ (120) ps for short (long) scintillator strips located at small (large) polar angles [14]. The detector granularity delivers a negligible contribution to the velocity resolution [15]. Thus, between midrapidity ($y_{cm} = 0.447$, $\beta_{cm} = 0.419$) and projectile rapidity ($y_{proj} = 0.894$, $\beta_{proj} = 0.713$) the velocity can be determined with a precision of $\sigma_\beta/\beta \simeq 0.4\% - 0.8\%$. Finally, from the velocity other kinetic quantities like the velocity $\mathbf{v}^{cm}$ and the particle momentum $\mathbf{p}^{cm}$ after transformation into the c.m. system of the colliding nuclei are deduced.

2.2 Event classification

About $4 \cdot 10^6$ central collisions are selected by demanding large charged-particle multiplicities to be measured in the outer Plastic Wall. The corresponding integrated cross section comprises about 8 % of the total cross

section. For this centrality class one would expect – within a geometrical picture – an average impact parameter of about 2 fm. Simulations which we have performed with the IQMD model [16] predict an average impact parameter of about 2.5 fm. For different particles with mass number A_{clus} Fig. 1 shows the phase space coverage of the detector components, outer Plastic Wall/Helitron, in the transverse momentum vs. rapidity plane for events selected by this centrality condition. Here, $p_t^0 = (p_t/A_{clus})/(p_{proj}/A_{proj})_{cm} = (\beta_t\gamma)/(\beta\gamma)_{cm}^{proj}$ and $y^0 = (y/y_{proj})_{cm} = (y/y_{cm} - 1)$ are the normalized transverse momentum and rapidity, respectively. Both observables are related to the corresponding projectile quantities in the c.m. frame of the colliding nuclei (with $(\beta\gamma)_{cm}^{proj} = 0.462$ for 400 A·MeV beam energy). It is obvious that for central collisions the Plastic Wall preferentially measures midrapidity particles with small velocities in the c.m. system ($\langle v^{cm}\rangle \simeq 0.25$ c $- 0.30$ c).

In previous investigations of central Au+Au collisions between 100 and 400 A·MeV beam energy it was found that the correlation function of pairs of intermediate mass fragments (IMF) is strongly affected by the collective directed sideward flow of nuclear matter [17,18]. This directed sideflow causes an enhancement of correlations at small relative momenta. The enhancement results from mixing of differently azimuthally oriented events; it vanishes if the events are rotated into a unique reaction plane, which is determined by the standard transverse momentum analysis [19]. This procedure is allowed because the geometrical acceptance and the detector efficiency are azimuthally symmetric. Thus, the technique of event rotation is applied also to the present data in order to prevent that such artificial correlations are introduced into the reference momentum distribution of the correlation function (cf. Sect. 2.3).

2.3 Correlation function

Let $Y_{12}(\mathbf{p_1}, \mathbf{p_2})$ be the coincidence yield of pairs of particles having momenta $\mathbf{p_1}$ and $\mathbf{p_2}$. Then the two-particle correlation function is defined as

$$1 + R(\mathbf{p_1}, \mathbf{p_2}) = \mathcal{N} \frac{\sum_{events,pairs} Y_{12}(\mathbf{p_1}, \mathbf{p_2})}{\sum_{events,pairs} Y_{12,mix}(\mathbf{p_1}, \mathbf{p_2})}. \quad (1)$$

The sum runs over all events fulfilling the above mentioned global selection criterion and over all pairs satisfying certain conditions given below. Event mixing, denoted by the subscript "mix", means to take particle 1 and particle 2 from different events. $\mathcal{N}$ is a normalization factor fixed by the requirement to have the same number of true and mixed pairs. The statistical errors of all the correlation functions presented below are governed by those of the coincidence yield, since the mixed yield is generated with two orders of magnitude higher statistics. The correlation function (1) is then projected onto the relative momentum $\mathbf{q}$,

$$\mathbf{q} = \mu\mathbf{v_{12}} = \mu(\mathbf{v_1^{cm}} - \mathbf{v_2^{cm}}). \quad (2)$$

Here, $\mathbf{v}_i^{cm}$ are the particle velocities calculated in the c.m. system of the colliding nuclei and $\mu = (m_1 m_2)/(m_1 + m_2)$ is the reduced mass of the pair. Besides the above described global event characteristics we use gate conditions on the angle ζ between $\mathbf{q}$ and the c.m. sum momentum of the particle pair $\mathbf{P}_{12}^{cm} = \mathbf{p_1^{cm}} + \mathbf{p_2^{cm}}$ and on the pair velocity $V = |\mathbf{P}_{12}^{cm}|/(m_1 + m_2)$. In order to exploit the full available statistics, two complement types of longitudinal correlation functions are generated. The forward and backward correlation functions are defined by cuts on the angle ζ, $\cos\zeta > 0$ and $\cos\zeta < 0$, respectively. This choice selects pairs with the longitudinal velocity component v_L (projection onto the pair velocity) of particle 1 being greater or smaller than the corresponding value of particle 2:

$$R^+(q) = 1 + R(q, \cos\zeta > 0) = 1 + R(q, v_{L,1} > v_{L,2}) \quad (3)$$

$$R^-(q) = 1 + R(q, \cos\zeta < 0) = 1 + R(q, v_{L,1} < v_{L,2}) \quad (4)$$

From the velocity resolution as estimated in Sect. 2 the corresponding q resolution is deduced. It is expected to amount to $\delta q = \mu\delta v_{12}$, where $\delta v_{12} = \sqrt{2\langle(\delta v^{cm})^2\rangle} = (0.006 \pm 0.002)$ c.

3 Analysis

3.1 Correlations from final-state interaction

The correlation function of two particles 1 and 2 which move with a pair velocity $\mathbf{V}$ is [3,20]

$$1 + R(\mathbf{p_1}, \mathbf{p_2}) = \int dt_1 dt_2 d\mathbf{r_1} d\mathbf{r_2} \rho_1(\mathbf{V}, \mathbf{r_1}, t_1)\rho_2(\mathbf{V}, \mathbf{r_2}, t_2) \times$$
$$|\Psi_{\mathbf{q}}(\mathbf{r_1} - \mathbf{r_2} - \mathbf{V}(t_1 - t_2))|^2, \quad (5)$$

where the density $\rho_{1,2}(\mathbf{r}, t)$ describes the probability to find particle 1 or 2, respectively, at time t and spatial coordinate $\mathbf{r}$ from which they are emitted (freeze-out configuration). The wave function $\Psi_{\mathbf{q}}$ describes the relative motion of the two particles with momenta $\mathbf{p_1}$ and $\mathbf{p_2}$. Since the interaction with the source is neglected this wave function depends only on the relative coordinate $\mathbf{r} = \mathbf{r_1} - \mathbf{r_2}$ and on the relative momentum $\mathbf{q}$ defined in (2). Here, we assume that the source functions $\rho_{1,2}$ do not depend on the velocity and have a Gaussian shape in space and time characterized by radius parameters $R_{1,2}$ and emission times $\tau_{1,2}$ while the duration of the emission is given by τ_0:

$$\rho_{1,2}(\mathbf{r}, t) = \frac{1}{4\pi^2 R_{1,2}^3 \tau_0} \exp[-\frac{r^2}{2R_{1,2}^2} - \frac{(t - \tau_{1,2})^2}{2\tau_0^2}]. \quad (6)$$

The simple form of (6) allows us to integrate over the center-of-mass coordinate $(m_1\mathbf{r_1} + m_2\mathbf{r_2})/(m_1 + m_2)$ and the time variables leading to

$$1 + R(\mathbf{p_1}, \mathbf{p_2}) = \int d^3r\, S(\mathbf{r}, \mathbf{V})|\Psi_{\mathbf{q}}(\mathbf{r})|^2 \quad (7)$$

with

$$S(\mathbf{r}, \mathbf{V}) = \frac{1}{(4\pi)^{3/2} R_0^2 D} \exp\Big(-\frac{1}{4D^2}\Big[(\mathbf{V}\Delta\tau + \mathbf{r})^2 + \frac{\tau_0^2}{R_0^2}(r^2 V^2 - (\mathbf{r}\cdot\mathbf{V})^2)\Big]\Big), \quad (8)$$

where we have introduced the time difference $\Delta\tau_{12}$ and an effective radius D by

$$\Delta\tau_{12} = \tau_1 - \tau_2, \quad D^2 = R_0^2 + (V\tau_0)^2, \quad R_0^2 = \frac{1}{2}(R_1^2 + R_2^2). \quad (9)$$

For a finite emission time difference $\Delta\tau_{12}$ the source function S depends on the sign of the scalar product $\mathbf{V}\cdot\mathbf{r}$. This asymmetry with respect to $\mathbf{r}$ is transferred to the correlation function (7) if the wave function $\Psi_{\mathbf{q}}$ contains terms of an odd power of the scalar product $\mathbf{q}\cdot\mathbf{r}$ which is possible for nonidentical particles.

The wave function $\Psi_{\mathbf{q}}$ is generated by partial wave expansion technique. To incorporate the spin degrees of freedom we use either spin-spin coupling (for p-p, d-p, t-p, ^{3}He-p, d-d, t-d, ^{3}He-d, and ^{3}He-t correlations) or l-s coupling (for α-p, α-d, α-t, and α-^{3}He correlations). Thus, the partial waves are classified by angular momentum and either total spin $s = s_1 + s_2$ or $j = l + s_2$. There is also an option to include partial waves with total angular momentum $J = l + s$ to describe dominant resonances.

The corresponding radial Schrödinger equations are solved using the Coulomb potential and Woods-Saxon potentials

$$V(r) = \frac{V_{ws}}{1 + \exp[-(r - R_{ws})/a_{ws}]}. \quad (10)$$

For each partial wave, the parameters R_{ws}, a_{ws}, V_{ws} are chosen such that the phase shifts are reproduced. As already mentioned in [7] it is important to find potentials which generate the correct dependence $d\delta/dq$ since the derivative of the phase shift is the relevant quantity in determining whether correlations are suppressed or enhanced. In most of the cases we make use of the parameters already obtained in [7,21,22]. (Note that for q values approaching a certain resonance positions q_i the phase shift has to amount 90 degrees.) For partial waves $l > 3$ the nuclear part of the potential is unimportant and has been neglected. In the case of p-p correlations the wave function has been generated using the Reid soft-core potential like in the standard Koonin model [3].

The wave function $\Psi_{\mathbf{q}}$ in (5) is the projection of the many body wave function of the two interacting clusters on their relative coordinates. The assumption made above that this wave function can be replaced by the partial waves could be violated for small distances $|\mathbf{r}_1 - \mathbf{r}_2|$ where many body effects are most important. Consequently, the potentials which are obtained by fitting the scattering phases might not be the optimum choice to produce the correlation function. E.g., the d-p correlation functions shown in Fig. 3 are too steeply increasing with relative momentum q. The agreement to the measurement is largely improved using the potential depth of 6 MeV instead of

the value of -13 MeV given in [7] for the $s = 3/2$, $l = 1$ partial wave. However, it is important to note that by changing this value the ratio R^+/R^- remains essentially unchanged. Therefore, we have decided to use potentials which are compatible with scattering phases avoiding the ambiguity which could arise by searching for new parameters in the very large parameter space.

3.2 Effect of radial flow

From (8) and (9) we observe that differences of the source extensions do not enter in the correlation function. This fact is a consequence of the isotropic distribution of the emission points which is independent of the particle momentum. However, in central nucleus-nucleus collisions a considerable amount of the bombarding energy is converted into flow energy. This collective expansion of nuclear matter sets in after the compression phase and can be observed as a decrease of the slope of the kinetic energy spectra. It causes a strong correlation between particle momenta and emission points. Therefore, we investigate in this section the influence of the flow on both the source radius and the emission time.

For this purpose we introduce into the emission function (6) a radial flow velocity. There is good experience [23] with the "nuclear Hubble scenario" which suggests a linear velocity profile. Such an assumption has furthermore the advantage that the function $S(\mathbf{r}, \mathbf{V})$ can be calculated analytically when using Gaussian density profiles. Thus, we write for particles with different mass numbers $A_{1,2}$

$$\rho_{1,2}(\mathbf{v}, \mathbf{r}, t) = N \exp[-\frac{r^2}{2R_{1,2}^2} - \frac{(t - \tau_{1,2})^2}{2\tau_0^2} - \frac{A_{1,2} m_0 (\mathbf{v} - \eta\mathbf{r})^2}{2T}], \quad (11)$$

where N is a normalization factor which ensures that the density is normalized to unity. In (11) the velocities of the particles are thermally distributed, characterized by the temperature T, around a radial flow velocity defined by the scaling parameter η.

The "nuclear Hubble constant" η is connected with the radial flow energy per nucleon

$$\epsilon_{flow} = \frac{m_0 \eta^2}{2}\langle r^2 \rangle = \frac{m_0 \eta^2}{2} 3 R_0^2. \quad (12)$$

The brackets imply averaging over the Gaussian density distribution, and the quantities m_0 and R_0 represent the nucleon rest mass and the mean radius, respectively.

Repeating the integration of (5) with the new functions $\rho_{1,2}$ one arrives at a similar relation for the source function S as (8), however the parameters R_0, D and $\Delta\tau_{12}$ of (9) have to be replaced by quantities indicated by an asterisk:

$$R_0^* = \sqrt{\frac{1}{2}\Big(\frac{R_1^2}{1 + \epsilon\tilde{r}_1^2 A_1} + \frac{R_2^2}{1 + \epsilon\tilde{r}_2^2 A_2}\Big)}, \quad (13)$$

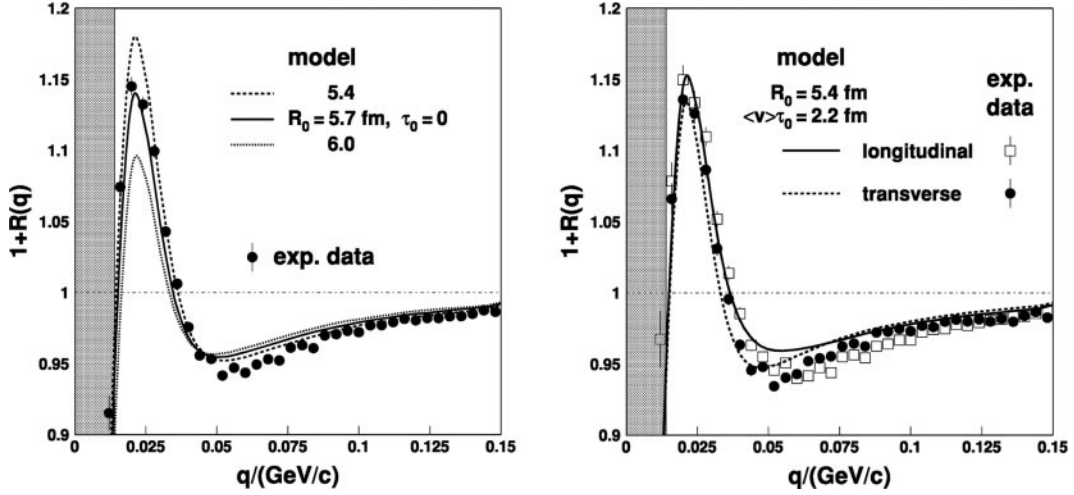$$D^* = \sqrt{(R_0^*)^2 + (V\tau_0)^2} \quad (14)$$

Fig. 2. Left panel: The experimental correlation function of proton pairs from central trigger events (dots). The hatched area indicates the unreliable region which may be contaminated by doubly counted scattered particles. The full line represents the model prediction for an emission from a Gaussian source of zero lifetime and radius $R_0 = 5.7$ fm. The dashed and dotted lines are the corresponding results for source radii which differ from the optimum one by -0.3 fm and +0.3 fm, respectively. Right panel: The transverse (dots) and longitudinal (squares) two-proton correlation functions compared to the model results (dashed and dotted lines) for finite lifetime $\langle V \rangle \tau_0 = 2.2$ fm and Gaussian radius $R_0 = 5.4$ fm

and

$$\Delta \tau_{12}^* = \tau_1^* - \tau_2^* = \Delta \tau_{12} + \Delta \tau_{12}^{flow} \qquad (15)$$

with

$$\tau_{1,2}^* = \tau_{1,2} - \frac{\tilde{r}_{1,2}^2 A_{1,2}}{1 + \epsilon \tilde{r}_{1,2}^2 A_{1,2}} \sqrt{\epsilon \frac{m_0}{T} R_0^2}, \qquad (16)$$

and

$$\Delta \tau_{12}^{flow} = -\left(\frac{\tilde{r}_1^2 A_1}{1 + \epsilon \tilde{r}_1^2 A_1} - \frac{\tilde{r}_2^2 A_2}{1 + \epsilon \tilde{r}_2^2 A_2} \right) \sqrt{\epsilon \frac{m_0}{T} R_0^2}. \qquad (17)$$

Here, we use the abbreviations $\tilde{r}_{1,2} = R_{1,2}/R_0$, and $\epsilon = \epsilon_{flow}/\epsilon_{therm}$ is the ratio of the radial flow energy ϵ_{flow} and the energy of the random thermal motion $\epsilon_{therm} = \frac{3}{2}T$.

From (13) one finds that the apparent source radius decreases monotonously with increasing energy ratio and particle mass. These observations do well compare with recent results of the investigation of the sensitivity of the proton-proton correlation to collective expansion in central Ni+Ni collisions at 1.93 A·GeV beam energy [15].

The essential result is that even if the two particles are produced at the same source region, $R_1 = R_2$, and at the same time, $\tau_1 = \tau_2$, the flow still causes an effective time difference $\Delta \tau_{12}^* = \Delta \tau_{12}^{flow}$ if the two particle masses are different. This can be understood as follows: For a given pair velocity $\mathbf{V}$ the heavier partner 1 with the smaller thermal velocity moves approximately with the flow velocity. This means that at freeze-out the heavier particle is located in the region around $\mathbf{r}_1 = \mathbf{V}/\eta$. Since the position of the lighter partner with the larger thermal velocity is Gaussian distributed around the center of the source, its mean location $\mathbf{r}_2$ is behind its heavier partner. Therefore, to have a strong final state interaction the lighter needs to start earlier. If they start however at the same time it seems as if the heavier particle would have started earlier, $\Delta \tau_{12}^* < 0$ in agreement with (15) and (16).

Furthermore, temporal and spatial differences in the source distribution add up to the effective emission times τ_i^* in (16) quite independently. Therefore, measuring the quantity $\Delta \tau_{12}^*$ alone will not allow us to disentangle the two different contributions. In the following analyses we will therefore differ two cases, namely first that all particles are emitted from the same source size ($R_i = R_0$) and second that they are emitted at the same time ($\tau_i = 0$) instant.

In our calculations which take the collective expansion into account we use an energy ratio of $\epsilon = 1$ and a temperature of $T = 37$ MeV. These values are compatible with values obtained in systematic flow studies [23] of central Au+Au collisions in case of 400 A·MeV beam energy. It should be mentioned that the flow correction $\Delta \tau_{12}^{flow}$ changes only slowly with the energy ratio ϵ because the temperature T in (17) is correlated with the flow energy ϵ_{flow} due to the requirement of energy conservation. Thus, even if for the present Ru+Ru system the ratio ϵ would be smaller than for the Au+Au system, one would find that the correction changes only marginally. E.g. a drastic reduction of ϵ by a factor of two leads to typical changes of $\Delta \tau_{12}^{flow}$ by about 20% only.

4 Results and comparison with model

4.1 The source extension

Figure 2 (left panel) shows the angle-integrated two-proton correlation function. As in previous fragment-fragment correlation analyses [17,18] an enhanced coincidence yield at very small relative angles is observed, which is due to double counting caused mainly by scattering in the scintillator strips. This disturbing yield is reduced drastically by the requirement to match the particle

hits on the Plastic Wall with the corresponding tracks in the forward drift chamber Helitron. However, mismatches of tracks and scattering processes especially at the wire planes of the chamber can give rise to a small amount of double counting, too. The remaining left-over of doubly counted scattered particles is eliminated by excluding, around a given hit, positions within a rectangular segment of azimuthal and polar angle differences $|\phi_1 - \phi_2| < 4^o$ and $|\theta_1 - \theta_2| < 2^o$. In order to keep the influence of the exclusion onto the correlation function as small as possible, the same procedure is applied to the uncorrelated background. However, GEANT simulations [24] have shown that at very small relative velocities $v_{12} < 0.03$ c a small bias of the correlation function cannot be excluded [15]. Though ratios of correlation functions as our forward/backward relation R^+/R^- are expected to be rather robust against such biases, the corresponding regions in the correlation functions are marked as hatched area and are not taken into consideration when comparing the experimental data with model predictions.

The experimental p-p correlation function is compared to the model for an emission from a source of zero lifetime and true Gaussian radius R_0 which corresponds to an r.m.s. radius of $R_{rms} \equiv \sqrt{\langle r^2 \rangle} = \sqrt{3} R_0$. The theoretical correlation function is folded with an experimental resolution function of Gaussian shape with the dispersion $\delta(q)$ as estimated in Sect. 2.3. The apparent reduction (13) of the source radius due to radial expansion effects as described in Sect. 3.2 (see also [15]) is estimated to $R_0^*/R_0 = 1/\sqrt{1+\epsilon} = 1/\sqrt{2}$. The best agreement of experimental data and model calculations is found for $R_0 = (5.7 \pm 0.3)$ fm. It is obvious that the appearance of the correlation peak at $q \simeq 20$ MeV/c allows the determination of the source radius with rather high sensitivity. This ^{2}He-resonance is the result of the common action of the enhancement due to the attractive nucleonic potential and the suppression due to both the mutual Coulomb repulsion and the antisymmetrization of the wave function. The ambiguity of the space and time extents of the proton emitting source can be resolved by constructing correlation functions with the relative momentum $\mathbf{q}$ being either perpendicular (transverse correlation function, here defined by $|\cos\zeta| < 0.5$) or parallel (longitudinal correlation function, here defined by $|\cos\zeta| > 0.5$) to the pair velocity $\mathbf{V}$. The result is given in the right panel of Fig. 2. We find a small suppression of the transverse correlations with respect to the longitudinal ones which is consistent with model predictions for the emission from a source of finite lifetime [3,6]. The best simultaneous fit around the correlation peaks (14 MeV/c $< q <$ 42 MeV/c) of both the transverse and longitudinal correlation functions delivers Gaussian parameters of the radius (after flow correction) and the emission duration of $R_0 = 5.4$ fm and $\langle V \rangle \tau_0 = 2.2$ fm, respectively. Obviously, the lifetime effect appears unimportant.

For the determination of the emission time differences in the subsequent section the source radius is kept fixed to a value of $R_1 = R_2 = R_0 = 5.7$ fm. For simplification the
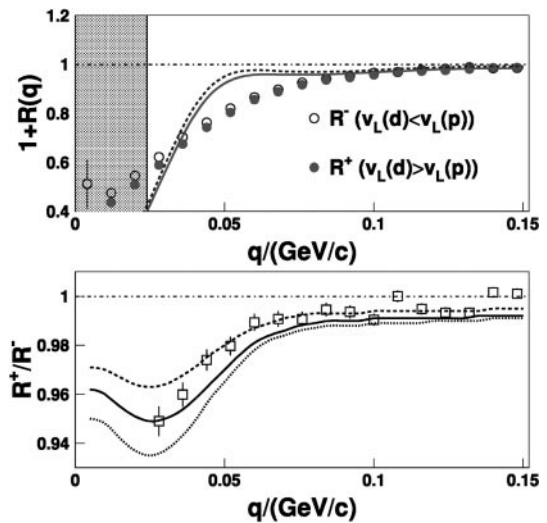

Fig. 3. Upper panel: Forward (full dots) and backward (open dots) longitudinal experimental correlation functions of d-p pairs. The hatched area indicates the unreliable region which may be contaminated by doubly counted scattered particles. The full and dashed lines give the corresponding model predictions with the time delay of Table 1. Lower panel: Ratio of forward/backward experimental correlation functions (open squares). The full line represents the ratio of the simulated correlation functions. The dashed and dotted lines give the model predictions for times differences deviating by -0.5 fm/c and +0.5 fm/c from the optimum one, respectively

duration of the emission τ_0 is set to zero. A finite value leads only to a rescaling of the effective radius in (14).

4.2 Emission time differences

Out of the ten different combinations of pairs of nonidentical particles which can be constructed from p, d, t, ^{3}He, and α particles there exist only two correlation functions which do not contain contributions of resonance decay products. These resonance-free correlation functions of deuteron-proton and ^{3}He-triton pairs are presented in Sect. 4.2.1. All other correlation functions contain resonance contributions of particle-unbound ground states or excited states of heavier clusters decaying into pairs of light charged particles. In case of the appearance of strong and narrow resonances in the q region of interest, the corresponding theoretical correlation functions are corrected for the experimental q resolution similarly as for p-p correlations.

4.2.1 Final-state interaction without resonances

Figure 3 gives the results of d-p correlations. The upper panel shows the forward (full dots) and the backward (open dots) correlation functions whereas the lower panel represents the ratio of both observables. The resonance-free correlation functions show a suppression at low relative momenta due to final-state Coulomb and nuclear
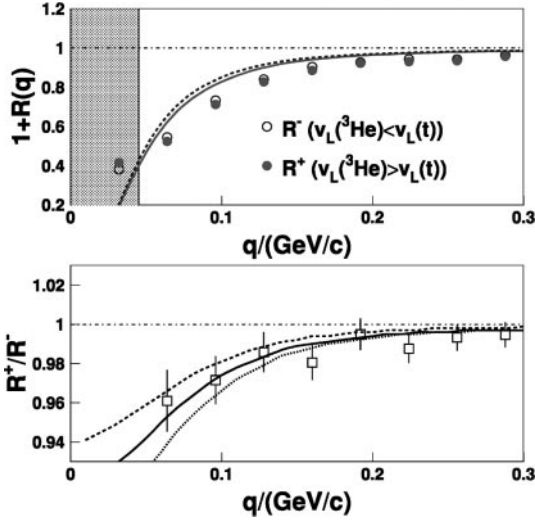
Fig. 4. The same as Fig. 3, but for ^{3}He-t correlations

Table 1. The apparent and the true values of the emission time difference as determined for all combinations of nonidentical charged-particle correlation functions. The source radii are fixed to $R_i = R_0$

light-charged particle combination 1 - 2	apparent time delay $\Delta\tau_{12}^*$ (fm/c)	true time delay $\Delta\tau_{12} = \tau_1 - \tau_2$ (fm/c)
d - p	1.7 ± 1	6.5 ± 1
t - p	-4.2 ± 3	3 ± 3
^{3}He - p	4.5 ± 1	11.7 ± 1
α - p	-2.6 ± 3	6 ± 3
t - d	-1.0 ± 1	1.4 ± 1
^{3}He - d	3.0 ± 1	5.4 ± 1
α - d	-2.0 ± 1	1.8 ± 1
^{3}He - t	1.7 ± 1	1.7 ± 1
α - t	-2.9 ± 1	-1.5 ± 1
^{3}He - α	4.4 ± 1	3.0 ± 1

interactions. Obviously, the suppression gets stronger in the case when deuterons are faster than protons (full dots in Fig. 3). This indicates that, on average, deuterons are being emitted later than protons. Quantitatively, the comparison with the model predictions yields an optimum time delay of $\Delta\tau_{d,p} = \tau_d - \tau_p = 6.5$ fm/c (full line in the lower panel). (The dashed and dotted lines in the lower panel of Figs. 3 and 4 should give an impression how the theoretical ratio R^+/R^- alters if the time delay is changed by -0.5 fm/c and +0.5 fm/c, respectively.) However, if one does not take into account the time shift due to the radial expansion of the participant zone the emission time difference would be determined as an apparent value which is much smaller (but still positive). Both the true and apparent time delays are summarized in Table 1. The given errors represent the typical band widths of time delay parameters around their optimum values which reproduce the experimental correlation function ratios R^+/R^- reasonably well.
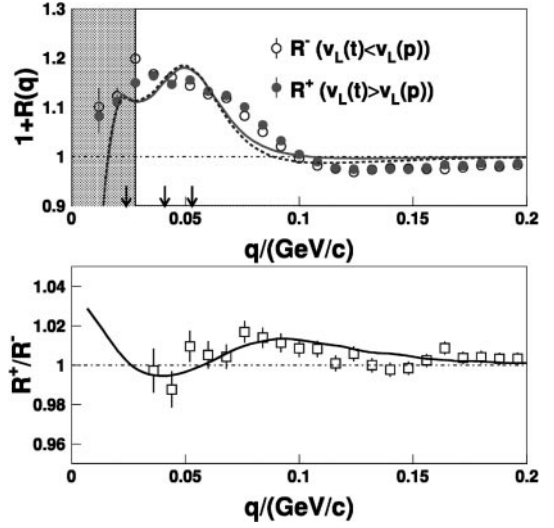

Fig. 5. Upper panel: Forward (full dots) and backward (open dots) longitudinal experimental correlation functions of t-p pairs. Positions of relevant resonances are marked as arrows. The hatched area indicates the unreliable region which may be contaminated by doubly counted scattered particles. The full and dashed lines give the corresponding model predictions with the time delay of Table 1. Lower panel: Ratio of forward/backward experimental correlation functions (open squares). The full line represents the ratio of the simulated correlations
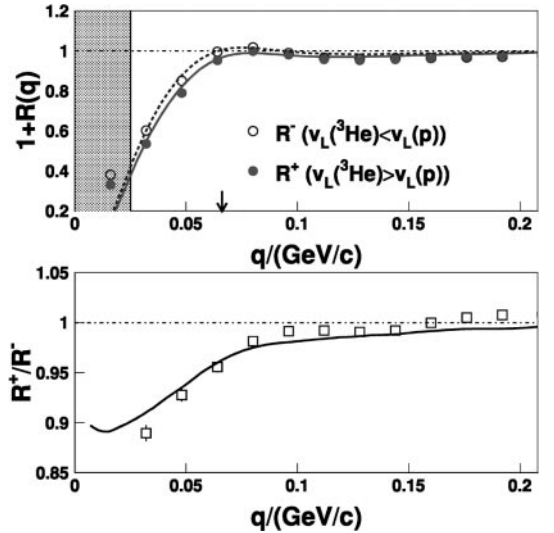

Fig. 6. The same as Fig. 5, but for ^{3}He-p correlations

Figure 4 shows the ^{3}He-t correlation functions and the corresponding forward/backward ratio. Since the masses of the two species are practically identical, this correlation function is the only one where – in case of equal source radii – the flow correction (17) vanishes and, consequently, the true and the apparent time delays are identical. Obviously, the ^{3}He particles are emitted slightly later than the tritons (about 1-3 fm/c, cf. Table 1).
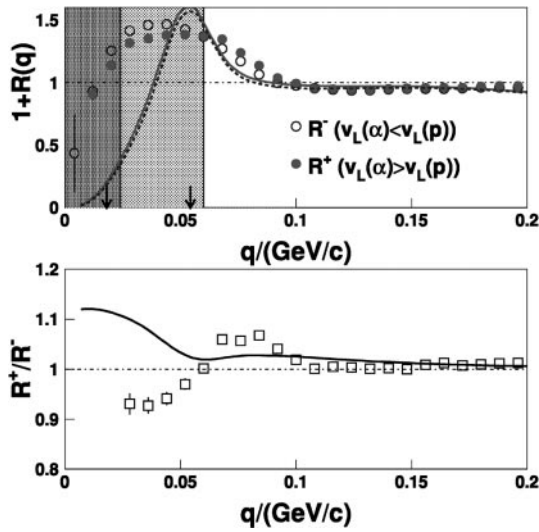
Fig. 7. The same as Fig. 5, but for α-p correlations. The dark hatched area indicates the unreliable region which may be contaminated by doubly counted scattered particles. The light hatched area gives the region which is supposed to be strongly contaminated by secondary decays of boron isotopes
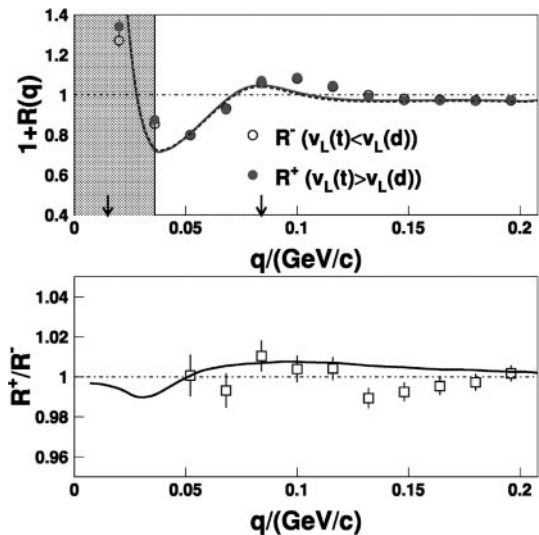

Fig. 8. The same as Fig. 5, but for t-d correlations

4.2.2 Final-state interaction with resonances

If a resonance contribution is dominating in the two-particle yield the ratio R^+/R^- necessarily is forced to unity for relative momenta q approaching the resonance value q_i. This is due to the fact that for pure two-body decays both particles are emitted at the same time (and position). Indeed, the experimental data show the expected behaviour (see arrow positions in Figs. 5-12).

Figure 5 shows the forward/backward longitudinal correlation functions of t-p pairs together with the corresponding ratio. The correlation function exhibits a broad peak which contains the contribution of the 1st excited state of ^{4}He ($E^* = 20.21$ MeV, $J^\pi = 0^+$, $\Gamma = 0.5$ MeV, $\Gamma_p/\Gamma = 1$, $q_1 = 23.6$ MeV/c) as well as the 2nd ($E^* =$

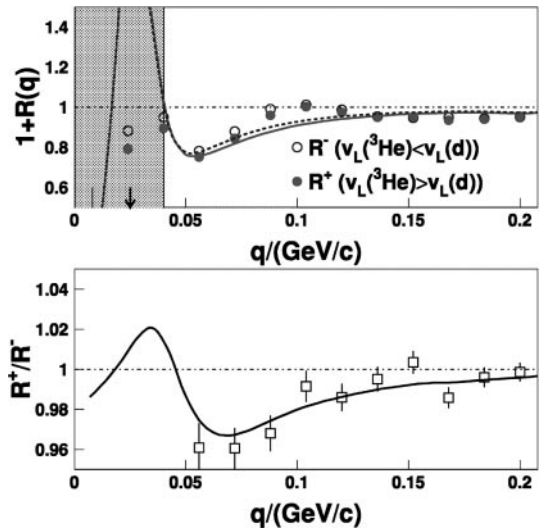**Fig. 9.** The same as Fig. 5, but for ^{3}He-d correlations

21.01 MeV, $J^\pi = 0^-$, $\Gamma = 0.84$ MeV, $\Gamma_p/\Gamma = 0.76$, $q_2 = 41.0$ MeV/c) and the 3rd one ($E^* = 21.84$ MeV, $J^\pi = 2^-$, $\Gamma = 2.01$ MeV, $\Gamma_p/\Gamma = 0.63$, $q_3 = 53.4$ MeV/c). The positions of the relevant resonances are marked by arrows. In the present case only the lowest three excited states of ^{4}He with widths $\Gamma < 2.1$ MeV are indicated. Other states in the energy region $E^* = 23 - 26$ MeV ($q = 70 - 90$ MeV/c) are much broader ($\Gamma > 5$ MeV, $\Gamma_p/\Gamma \simeq 0.5$). Obviously, from the lower part of the figure one would conclude a negative time delay $\Delta\tau^*_{t,p}$. However, the radial flow correction (17) overcompensates this apparent time difference and leads to a positive value (cf. Table 1). Due to the possible contribution of higher lying resonances of ^{4}He which are not taken into account in the model description, a rather large error is appended to the time delay.

Figure 6 represents the results for ^{3}He-p correlations. One broad maximum shows up which is related to the particle-unbound ground state of ^{4}Li ($J^\pi = 2^-$, $\Gamma = 6$ MeV, $q_0 = 66.0$ MeV/c). An unquestionably positive time delay $\Delta\tau_{^3He,p}$ is deduced from the correlation function ratio R^+/R^-. Here, about 60 % of the true time difference given in Table 1 arise from the radial flow correction (17).

Figure 7 gives the α-p correlations. The origin of the broad bump is not fully understood. The main contribution results from the decay of the particle-unbound ground state of ^{5}Li ($J^\pi = \frac{3}{2}^-$, $\Gamma = 1.5$ MeV, $\Gamma_p/\Gamma = 1$, $q_0 = 54.3$ MeV/c). Most probably, the bump contains additional contributions [25-27] which cannot be separated experimentally from the ^{5}Li resonance. One contribution is expected at $q \simeq 16$ MeV/c. It corresponds to the three-body decay of ^{9}B(g.s.) $\rightarrow$ p + ^{8}Be(g.s.) $\rightarrow$ p + α + α, where only one of the α particles is detected together with the proton. In addition, the four-body decay of ^{10}B$^* \rightarrow$ p + ^{9}Be(1.69 MeV) $\rightarrow$ p + n + ^{8}Be(g.s.) $\rightarrow$ p + n + α + α can contribute to the broad maximum as was deduced at a comparably low beam energy of 40 A·MeV [27]. In

the present case such a contribution cannot be ruled out since a considerable production of 0.3 boron clusters per event was found in central Au+Au reactions at 400 $A\cdot$MeV beam energy [23].

Due to the large lifetime of the ^{8}Be ground state ($\Gamma = 6.8$ eV) the protons – a priori – are emitted earlier than the α particles. Thus, for relative momenta $q \simeq 0 - 60$ MeV/c one necessarily expects stronger final-state interaction if $v_L(\alpha) > v_L(p)$ and consequently $R^+/R^- < 0$. Indeed, the experimental data follow the predicted trend. However, since the model description does not incorporate two-stage decays, a reliable time difference can only be extracted for q values well above the resonance q_0. Keeping in mind that the sensitivity of the correlation function to a variation of the model parameter $\Delta\tau_{12}$ decreases for increasing q, the deduced value is affected with a rather large error. Thus, the time difference derived from the α-p correlation function will enter with negligible weight into the procedure used to determine the emission-time sequence of the different particle species (cf. Sect. 4.3).

Two resonances affect the t-d correlation function (Fig. 8). The first one which is not resolved experimentally corresponds to the 16.75 MeV excited state of ^{5}He ($J^\pi = \frac{3}{2}^+$, $\Gamma = 76$ keV, $q_1 = 10.8$ MeV/c). The second one is due to the state at 19.8 MeV ($J^\pi = (\frac{3}{2}, \frac{5}{2})^+$, $\Gamma = 2.5$ MeV, $q_2 = 83.5$ MeV/c). From the lower part of the figure it is obvious that the apparent time delay is close to zero. Indeed, the model fits well the data for a true emission time difference (cf. Table 1) which – to a large extent – is due to the contribution of the radial flow correction (17).

The ^{3}He-d correlations in Fig. 9 appear very similar to the t-d correlations. The correlation function contains one strong peak due to the 16.66 MeV state of ^{5}Li ($J^\pi = \frac{3}{2}^+$, $\Gamma = 0.3$ MeV, $q_1 = 24.8$ MeV/c). Other broader states are at 18.0 MeV ($J^\pi = \frac{1}{2}^+$, $\Gamma \simeq 5$ MeV, $q_2 = 60.3$ MeV/c) and at 20.0 MeV ($J^\pi = (\frac{3}{2}, \frac{5}{2})^+$, $\Gamma = 5$ MeV, $q_3 = 90.2$ MeV/c). Only the narrow 16.66 MeV state is taken into account in the model. In contrast to the t-d correlations, we find a clearly positive apparent time delay $\Delta\tau^*_{^3\mathrm{He,d}} \simeq 3$ fm/c which increases nearly by a factor of 2 due to the radial flow correction.

The α-d correlation function shown in the upper panel of Fig. 10 is governed by a strong resonance due to the narrow 2.186 MeV state of ^{6}Li ($J^\pi = 3^+$, $\Gamma = 24$ keV, $q_1 = 42.2$ MeV/c). Another state is at 4.31 MeV ($J^\pi = 2^+$, $\Gamma = 1.7$ MeV, $q_2 = 84.2$ MeV/c). Obviously, from the lower part of the figure one would conclude a negative time delay $\Delta\tau^*_{\alpha,\mathrm{d}}$. However, for the present case the radial flow correction (17) overcompensates the apparent time difference leading to a positive value (cf. Table 1). As a by-product, the strong 3^+ resonance of ^{6}Li in the correlation function can serve for an independent determination of the q resolution. A Gaussian fit to the difference spectrum of true and normalized mixed yields in the region 20 MeV/c $< q <$ 60 MeV/c delivers a dispersion of $\delta v_{12} = \delta q/\mu = 7.1$ (MeV/c)$/\mu = 0.0057$ c in good agreement with the estimate given in Sect. 2.3.
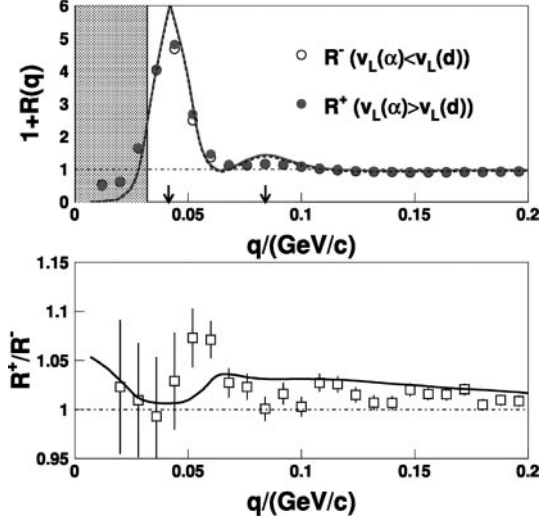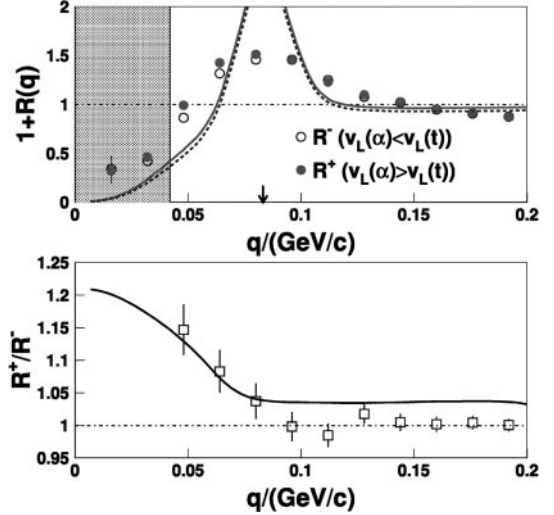
Fig. 10. The same as Fig. 5, but for α-d correlations

Fig. 11. The same as Fig. 5, but for α-t correlations

The α-t correlation function given in Fig. 11 is characterized by a broad maximum due to the 4.63 MeV state of ^{7}Li ($J^\pi = \frac{7}{2}^-$, $\Gamma = 93$ keV, $q_1 = 83.4$ MeV/c). Other states are at 6.68 MeV ($J^\pi = \frac{5}{2}^-$, $\Gamma = 880$ keV, $q_2 = 116.4$ MeV/c) and at 7.46 MeV ($J^\pi = \frac{5}{2}^-$, $\Gamma = 89$ keV, $q_3 = 126.7$ MeV/c). Only the 4.63 MeV state is taken into account in the model. The deduced time delay $\Delta\tau_{\alpha,t}$ is apparently negative; it is reduced by about 50 % when taking into account the radial flow correction (cf. Table 1).

The ^{3}He-α correlation function in Fig. 12 is dominated by the 4.57 MeV state of ^{7}Be ($J^\pi = \frac{7}{2}^-$, $\Gamma = 175$ keV, $q_1 = 98.0$ MeV/c). Here, both the deduced apparent and true time delays $\Delta\tau_{^3\mathrm{He},\alpha}$ are found positive (Table 1) and differ only by about 1.5 fm/c. Similarly to the α-t correlations the small flow correction is a result of the small relative mass difference of the particles.
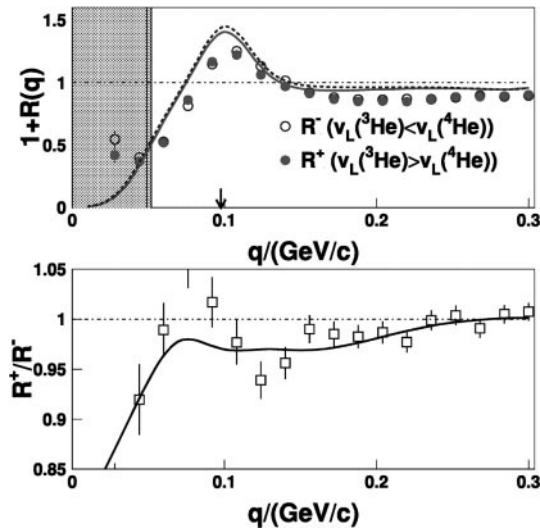
Fig. 12. The same as Fig. 5, but for ^{3}He-α correlations

4.3 Discussion

Finally, the redundancy of the ten different pair-wise time differences obtained above allows one to fix rather reliably the emission-time sequence of the light charged particles. The optimum sequence is derived from a least-squares solution of the set of linear equations for the time delays given in Table 1. (Note that, the deduced χ^2 per degree of freedom of 1.1 does not carry quantitative information on the quality of the regression since the errors of the individual time delays are not real standard deviations.) The different contributions are weighted by the inverse squares of the given errors. If one excludes from the fit a few of the time differences (e.g. those which are affected with large errors like in the case of α-p and t-p correlations) the result changes only marginally. For a fixed source radius, the most probable time order of the emission is found as follows (cf. Table 2): On the average, protons are emitted first whereas ^{3}He particles are emitted last (after about 11 fm/c). The other particles show up in between. Deuterons are emitted about 6 fm/c after protons. After that, the α particles are emitted and then the tritons follow. However, the differences between the emission times of these species are found in the order of 1 fm/c only (note: 3 fm/c = 10^{-23} s).

As a consequence of the duality of space and time coordinates, the time delays can be transformed into position differences. When assuming a common emission time for all particles, the time sequence translates into the emission from different source radii R_i according to (16) as a consequence of the radial flow. A very similar procedure as described above for the emission times at unique source size leads to the average radii for the emission at the same time instant. The results are summarized in the 3rd row of Table 2. Now, the protons, which are emitted earliest in the time-ordered picture, would come from the most extended source ($R_{rms} = \sqrt{3}R_0 \simeq 10$ fm) whereas the clusters (with the exception of α particles, which obviously play a special role) are emitted from source radii

Table 2. The 2nd row gives the emission times (relative to that of the protons) for fixed source radii $R_i = R_0$ of d, t, ^{3}He, and α particles as derived from a weighted regression of the ten linear equations for the pair-wise time delays given in Table 1. The 3rd row gives the complementary information of different source radii (normalized to that of the proton source $R_p = R_0$) if the emission takes place at the same time instant

	d	α	t	^{3}He
$\frac{\tau_i - \tau_p}{fm/c}$	6.3 ± 0.8	7.7 ± 0.9	8.5 ± 0.9	11.1 ± 0.8
R_i/R_p	0.63 ± 0.04	0.54 ± 0.05	0.53 ± 0.05	0.44 ± 0.04

which decrease with increasing mass. Thus, the size of the emission sources of the d, α, t and ^{3}He particles would be about 63%, 54%, 53% and 44% of that of the protons, respectively.

This finding is in qualitative agreement with the results of an earlier investigation [28] of the cluster formation process in central Au+Au collisions at 250 A·MeV. There, the authors compare the experimental data with predictions of a model which describes the hydrodynamic isotropic expansion of an ideal nucleonic gas and the clustering by statistical disassembly. The model predicts a breakup which, with elapsing time, starts at the exterior and evolves to smaller radii. The heavier fragments are found to arise from smaller source radii than the light particles.

The α particles do not follow completely the systematic trend established above. One reason for this violation of the emission order with increasing mass might lie in the fact that this (strongly bound) particle species, at least partially, is made of nucleons which were initially correlated either in the target or projectile nucleus [29]. Such preformed clusters would carry to some extent a memory of the entrance channel.

We have studied, whether the emission time difference of protons and composite particles can be explained by calculations we have performed with the IQMD transport model [16]. For a central ($b < 4$ fm) reaction of Ru+Ru we have investigated the distribution of the time instants at which the particles pass through the surface of a sphere in coordinate space. Only particles coming from the participant zone have been selected by a cut on the c.m. polar angle $|\tan\Theta_{cm}| > 1$. Since correlation functions are sensitive to particle pairs with small relative momenta only, in addition, we have to demand that the velocities of both particles be the same. The time distributions of all the light charged particles are found almost symmetric and exhibit – within the statistical errors – identical mean values. Alternatively, the cross check of the radial distributions of particles with equal velocities at a unique time reveals no differences of the mean radii. This finding is not surprising since most of the transport codes generate composite particles by coalescence. Indeed, such a method provides the composite particles with the same space-time distribution as the nucleons of equal velocity.

5 Summary

In conclusion, we have presented experimental correlation functions of nonidentical light charged particles produced in central collisions of Ru(Zr)+Ru(Zr) at 400 A·MeV.

For the first time an emission order of p, d, α, t, and ^{3}He particles has been set up by comparing correlations of particles with relative momenta parallel and anti-parallel to the center-of-mass velocity of the pair. Collective radial expansion of the participant zone leads to an apparent reduction of the source radius and to shifts of the emission times. Correcting for both effects typical time delays of a few fm/c were obtained. The deduced space-time differences of the light-charged-particle emission sources allow two complementary interpretations. If the source radius is fixed the composite particles are emitted at later times than protons. Alternatively, if the emission time is fixed, the clusters are emitted from smaller sources than protons. As a result of the duality of space and time coordinates, these two scenarios cannot be distinguished from each other.

References

1. G.I. Kopylov and M.I. Podgoredsky, Yad. Fiz. **18** (1973) 656 [Sov. Journ. Nucl. Phys. **18** (1973) 336]
2. G.I. Kopylov, Phys. Lett. B **50** (1974) 472
3. S.E. Koonin, Phys. Lett. B **70** (1977) 43
4. S. Pratt, Phys. Rev. Lett. **53** (1984) 1219
5. S. Pratt, Phys. Rev. D **33** (1986) 72; ibid., p. 1314
6. S. Pratt ans M.B. Tsang, Phys. Rev. C **36** (1987) 2390
7. D.H. Boal, C.K. Gelbke, and B.K. Jennings, Rev. Mod. Phys. **62** (1990) 553
8. C.J. Gelderloos and J.M. Alexander, Nucl. Instr. Meth. **A349** (1994) 618
9. C.J. Gelderloos et al., Phys. Rev. Lett. **75** (1995) 3082
10. R. Lednický, V.L. Lyuboshitz, B. Erazmus, and D. Nouais, Phys. Lett. B **373** (1996) 30
11. S. Voloshin, R. Lednický, S. Panitkin, and Nu Xu, Phys. Rev. Lett. **79** (1997) 4766
12. D. Miśkowiec, nucl-ex/9808003
13. F. Rami, Y. Leifels, B. de Schauenburg, FOPI collaboration, to be submitted to Phys. Rev. Lett.; Y. Leifels et al., GSI Scientific Report 1997, GSI 98-1 (1998) 57; B. de Schauenburg, F. Rami, and P. Wagner, ibid, p. 58; F. Rami, Proc. of the 14th Winter Workshop on Nuclear Dynamics, Snowbird, Utah, 1998.
14. A. Gobbi et al., FOPI collaboration, Nucl. Instr. Meth. **A324** (1993) 156; J. Ritman for the FOPI collaboration, Nucl. Phys. (Proc. Suppl.) **B44** (1995) 708
15. R. Kotte et al., FOPI collaboration, Z. Phys. A **359** (1997) 47
16. S.A. Bass, C. Hartnack, H. Stöcker and W. Greiner, Phys. Rev. C **51** (1995) 3343
17. B. Kämpfer et al., FOPI collaboration, Phys. Rev. C **48** (1993) R955
18. R. Kotte et al., FOPI collaboration, Phys. Rev. C **51** (1995) 2686
19. P. Danielewicz and G. Odyniec, Phys. Lett. B **157** (1985) 146
20. W. Bauer, C.K. Gelbke, and S. Pratt, Ann. Rev. Nucl. Part. Sci. **42** (1992) 77; and references cited therein
21. D.H. Boal and J.C. Shillcock, Phys. Rev. C **33** (1986) 549
22. B.K. Jennings, D.H. Boal, and J.C. Shillcock, Phys. Rev. C **33** (1986) 1303
23. W. Reisdorf et al., FOPI collaboration, Nucl. Phys. **A 612** (1997) 493
24. Application Software Group, CN Division, CERN: GEANT3.21, CERN Program Library Long Writeup W5013 (1994)
25. J. Pochodzalla et al., Phys. Lett. B **161** (1985) 275
26. Zhi Yong He et al., Nucl. Phys. **A 620** (1997) 214
27. R.J. Charity et al., Phys. Rev. C **52** (1995) 3126
28. M. Petrovici et al., FOPI collaboration, Phys. Rev. Lett. **74** (1995) 5001
29. P.B. Gossiaux and J. Aichelin, Phys. Rev. C **56** (1997) 2109